# Revision 3

# K isotopic fractionation in K-feldspar: Effects of mineral chemistry

Shanke Liu[a*], Wenjun Li[a], Benxun Su[a, b], Qiqi Pan[b, c], Meng Yuan[b, c], Patrick Asamoah Sakyi[d]

a Key Laboratory of Mineral Resources, Institute of Geology and Geophysics, Chinese Academy of Sciences, Beijing 100029, China

b University of Chinese Academy of Sciences, Beijing 100049, China

c State Key Laboratory of Lithospheric Evolution, Institute of Geology and Geophysics, Chinese Academy of Sciences, Beijing 100029, China

d Department of Earth Science, College of Basic and Applied Sciences, University of Ghana, P.O. Box LG 58, Legon-Accra, Ghana

* Corresponding author, e-mail: liushanke@mail.iggcas.ac.cn.

**ABSTRACT**

Controlling factors of potassium (K) isotopic fractionation in K-feldspar remain poorly constrained. In this study, we analyzed the K isotopic compositions of eleven K-feldspar samples

from diverse lithological compositions. Degree of Al/Si order ranged from 0.22 to 0.94 (1.0 = completely ordered). Analyzed samples are mixtures of K-feldspar (>70 wt%) and coexisting albite. The relative contribution of $K_2O$ from the K-feldspar phase of the sample was over 98%, indicating that the K isotopic composition ($\delta^{41}K$) derives mainly from K-feldspar and hence reflects its behavior. The $\delta^{41}K$ values of these samples range from -0.710 to -0.075‰, which are slightly correlated with the degrees of Al/Si order. The correlations of $\delta^{41}K$ with $SiO_2$ and $Al_2O_3$ contents and the corresponding Al/Si mole ratios reveal that Al and Si play a significant role in the K isotopic behavior of K-feldspar. The correlations of $\delta^{41}K$ with $SiO_2$ and $Al_2O_3$ contents are attributed to the difference in K-O bond strengths. Compared to K-feldspar, the K content could be a better proxy for constraining the $\delta^{41}K$ of plagioclase. Our results demonstrate that the $\delta^{41}K$ of K-feldspar is dependent on its mineral chemistry and its K isotopic composition may be insensitive to other factors, such as the source heterogeneity. The inference is further confirmed by comparing the $\delta^{41}K$ values in this study with published $\delta^{41}K$ values of K-feldspar from different sources.

**Key words:** K isotopes; K-feldspar; Al/Si order; Bond length; Al/Si mole ratio.

## INTRODUCTION

Potassium (K) is a highly incompatible lithophile element, and a highly soluble and biophile element that plays an important role in many biological processes (Hollabaugh, 2007; Stosch, 1998). Many analytical innovations have allowed K isotopic measurements (Hu et al., 2018; Li et al., 2016, 2022; Morgan et al., 2018; Wang and Jacobsen, 2016) which have enabled the evaluation of a variety of geochemical processes (Wang et al., 2020, 2021). Whereas available K

45 isotopic data have been mainly derived from whole rock analyses, it is imperative to emphasize
46 that K-rich minerals within rocks control the overall K isotopic variations, a facet that has yet to
47 receive adequate attention. Notably, studies of igneous rocks have indicated that the fractional
48 crystallization of K-rich phases such as mica and K-feldspar holds the potential for playing a
49 pivotal role in driving K isotopic variation (Ding et al., 2023; Su et al., 2023). The isotopic data
50 sourced from these K-rich minerals have the capacity to enrich our comprehension of geological
51 processes when merged with other geochemical and petrological tools. Moreover, K-feldspar, in
52 which K is an major element, is a common mineral in the crust and plays an essential role in
53 magma generation, crustal magma evolution, and subsequent alteration (Brown and Parsons,
54 1994; Černý, 1994; Vernon and Paterson, 2008; Yuan et al., 2019). By examining the isotopic
55 signatures in K-feldspar, we may gain further insights into geological phenomena that otherwise
56 remain concealed.

57 To date, a limited number of K-feldspar samples, mainly from pegmatites and other igneous
58 rocks, have been studied globally, exhibiting a wide $\delta^{41}K$ range from -1.19 to -0.08‰ (e.g., Chen
59 et al., 2019; Hu et al., 2021; Huang et al., 2023; Kuhnel et al., 2021; Morgan et al., 2018; Xu et al.,
60 2019). The previous studies were mainly aimed at: (i) developing a new methodology for high-
61 precision K isotope measurement in K-bearing minerals and (ii) understanding K isotopic
62 compositions of different mineral phases and their role during magmatic differentiation. Morgan et
63 al. (2018) analyzed a broad set of samples, but they did not provide conclusive evidence for any
64 particular mechanisms responsible for naturally-occurring K isotopic fractionation. They
65 speculated that magma fractionation, along with diffusion, may explain the variability in the
66 measured $^{41}K/^{39}K$ ratios. Very recent studies on potassium isotopes of K-rich minerals, such as

plagioclase, K-feldspar and mica, obtained from granitoids in cogenetic magmatic suites, show both large-scale intra-mineral and inter-mineral fractionations, which mainly depend on the K content and K-O bond length (Huang et al., 2023; Kuhnel et al., 2021). These studies highlighted application of K isotope geochemistry as a new tracer due to the existence of large K isotope fractionation during granitic magmatism.

K-feldspar is commonly divided into three principal varieties, namely microcline, orthoclase, and sanidine in the order of increasing crystallization temperature from ~200 to >1000 °C (Smith and Brown, 1988a; Brown and Parsons, 1989; Parsons, 2010). The division of K-feldspar is based on the state of order or disorder. The formation temperature and subsequent cooling history dictate the degree of Al/Si order among the four-membered rings of the $TO_4$ tetrahedra of K-feldspar (Smith and Brown, 1988b). Generally, the degree of Al/Si order increases from sanidine and orthoclase to microcline, with decreasing crystallization temperature (Brown and Parsons, 1989; Parsons, 2010). Ordering during subsequent subsolidus processes is an important factor. Considering the fact that stable isotope fractionation in general is temperature-dependent and the equilibrium fractionation between two phases generally decreases with increasing temperature (Oneil, 1977, 1986; Schauble, 2004; Urey, 1947), it is reasonable to speculate that theoretically, K isotopes are likely to be highly fractionated among the feldspar varieties (Kuhnel et al., 2021; Li et al., 2019a, 2019b; Zeng et al., 2019). Therefore, the change in the degree of Al/Si order may directly correlate with the K isotopic fractionation in K-feldspar. Additionally, modifications in Na or Ca content could lead to variations in the K-O bond length within feldspar. Consequently, an increase in Na or Ca content is anticipated to be associated with elevated proportions of the heavier $^{41}K$ isotope due to the shorter K-O bond length (Kuhnel et al. 2021; Li et al., 2019b, Zeng

et al., 2019).

In this study, we attempt to understand the key factors in generating measured K isotopic variation in feldspars of different composition by investigating a suite of K-feldspar samples constituting mostly >80 wt% K-feldspar phase. These samples are characterized by variable degrees of Al/Si order and K/(K+Na+Ca) mole ratios. Our results indicate that K isotopic variation in these samples is dependent on the change of Al/Si mole ratio, which dictates the change of K-O bond length of feldspars.

## SAMPLE DESCRIPTIONS

Eleven samples, six microcline, four orthoclase, and one sanidine, were collected from seven districts in China. These samples were studied as raw materials for artificial K-fertilizers or soil conditioners (Hellmann et al., 2021; Zhai et al., 2021), and their degrees of Al/Si order have already been determined (Liu and Zhai, 2021). All samples were mined within the past ten years, and their salient features are described below.

The six microcline-containing samples were collected from four different locations. Microcline in these samples is light pink in color and appears mostly as euhedral-subhedral crystals with grain size in the range of 1~20 mm. Sample SX-1 was separated from a granite porphyry (1786 Ma; Cui et al., 2010) in the Xiong'er Volcanic Province of the Xiong'ershan region, Henan Province. The granite porphyry mainly contains microcline (~40% in volume), quartz (~20%), plagioclase (~20%), and muscovite (5%). Samples LS-1 and LS-2 are from granitic pegmatite veins in Lingshou County, Hebei Province. The granitic pegmatite body is light pink with massive structure and has a mineral assemblage of microcline (80%) and others (20%), including quartz and small amounts of limonite and vermiculite. The microcline phenocrysts show

lattice twinning texture. Sample WLST-1 is from a quartz porphyry in the Weilasituo area of the southern Great Xing'an range (131 Ma; Zhang et al., 2019). The quartz porphyry is gray-white and has characteristics of cryptocrystalline matrix and a massive structure; amazonitization is well developed and microcline constitutes ~65% in volume, along with ~30% quartz and ~5% muscovite. Samples TYG-3 and TYG-4 were collected from Late Permian granites (253 Ma; Guo, 2019) in Chifeng city, Inner Mongolia. The granites are grayish-white or light pale-red in color with medium to fine-grained texture and massive structure. The mineral compositions are microcline (~50%), plagioclase (~28%), quartz (~20%), and biotite (~2%).

Samples CSY-1, CSY-2 and CSY-3 were collected from a syenite porphyry (148 Ma; Wu et al., 2017) in Chifeng city, Inner Mongolia. The syenite porphyry is grayish-white or light pale-red. It contains orthoclase (~70%) with grain size of 2-15 mm, plagioclase (~10%) with grain size of 3-10 mm, and quartz (~20%) with grain size of 1-4 mm. Sample CHG-12 was collected from a granite porphyry (252 Ma; Meng et al., 2013) in Chifeng city, Inner Mongolia. The granite porphyry is light pale-red, and its phenocrysts are mainly composed of plagioclase, orthoclase, and quartz.

The sanidine sample FHS-1 was collected from an ultra-hypabyssal granite porphyry (27.6 Ma; Wu et al., 2007), located 50 km west of the Fenghuo Mountain in Qinghai Province. The granite porphyry is fresh and grayish, and is mainly composed of sanidine (20%), with the remaining 80% composed of quartz and pyroxene. The sanidine phenocrysts, typically measuring 0.5–2 mm in size, display a zoning pattern, characterized by well-defined core regions and discernible boundaries, along with Carlsbad twins.

## ANALYTICAL METHODS

The samples were crushed and then hand-picked under an optical microscope. Subsequently, each sample was dry-ground with a mortar and pestle, and further removal of extraneous phases was done with heavy liquid separations. K-feldspar can be efficiently separated by blending liquids with specific gravity values customized for it and utilizing centrifugal separation. After the treatment with heavy liquids, grains were sieved and those < 74 μm were used for analysis.

**X-ray powder diffraction**

X-ray powder diffraction (XRPD) was applied to calculate the degree of Al occupancy in K-feldspar. The XRPD patterns of the bulk samples were collected using a PANalytical X'Pert Pro diffractometer with Cu$K\alpha$ radiation at 40 kV and 40 mA, a 0.0167° step size over a 2θ range of 10-90° at the Institute of Geology and Geophysics, Chinese Academy of Sciences (IGGCAS). The XRPD data were fitted and refined by the Rietveld method using the computer program package GSAS (Larson and Von Dreele, 2004) and its graphical interface EXPGUI (Toby, 2001). The instrumental parameter file was obtained from the XRPD pattern of $LaB_6$ standard (SRM 660b, National Institute of Standards and Technology, USA). The starting atomic coordinates, cell parameters, equivalent isotropic displacement parameters, and space groups of sanidine, orthoclase, microcline, albite, quartz, and kaolinite were based on structural data from Gering (1985), Colville and Ribbe (1968), Dal Negro et al. (1978), Wenk and Kroll (1984), d'Amour et al. (1979), and Bish (1993), respectively. Because of the preferred orientation of feldspar powder, the spherical harmonics function and March-Dollase function were used for K-feldspar and albite, respectively. Considering the resolution of the XRPD data and the quantities of atom parameters included in the Rietveld model, only cell parameters of all phases were optimized to avoid a pseudo convergence. The degree of Al/Si order (Z) of K-feldspar phase can be obtained from the

parameters of K-feldspar unit cell, and the detailed method has been described by Liu and Zhai (2021).

**Determination of chemical composition**

To determine the chemical compositions of the eleven bulk samples, a mixture of individual powder samples (0.5 g) and $Li_2B_4O_7$ + $LiBO_2$ (5 g) was heated and fused into a glass disc. The composition of the bulk sample was then analyzed by X-ray fluorescence spectroscopy (XRF) using a Shimadzu XRF 1500 sequential spectrometer (Shimadzu Corporation, Japan) at the IGGCAS. GSR-1, GSR-2, and GSR-3 were used to monitor the preparation process and instrument status, and the analytical precision of the sum of chemical compositions was controlled to within ±1%.

The analyzed samples were found to be mixtures mainly composed of K-feldspar and albite phases, despite the steps taken in mineral separation. To supplement the bulk sample analyses, individual grains were analyzed using a JEOL JXA8100 electron microprobe at the IGGCAS. Samples were analyzed using a voltage of 15 kV, a beam current of 20 nA, a spot size of 1 μm, and a 10–30 s peak counting time. The natural minerals and synthetic oxides used for calibration are as follows: diopside (Ca, Si, and Mg), albite (Na and Al), rutile (Ti), bustamite (Mn), K-feldspar (K), $Fe_2O_3$ (Fe), chromite (Cr), and NiO (Ni). A program based on the ZAF procedure was used for data correction. The estimated analytical precision of major oxide measurements is ±2%.

**Determination of K isotopes**

Potassium isotope analyses were conducted at the Metallogenic Elements and Isotopes Lab at the IGGCAS, following the protocol described in Li et al. (2022). Approximately 1 mg of the

177 powdered bulk sample was weighed and digested using a mixture of concentrated $HNO_3$ and HF.
178 The digested solutions were evaporated to dryness and then treated sequentially with aqua regia
179 and 6 mol $L^{-1}$ $HNO_3$. After evaporating the solutions, the final residues were fully dissolved twice
180 in 0.5 mol $L^{-1}$ $HNO_3$ prior to column separation. The sample solution was loaded onto a pre-
181 conditioned 2 mL Bio-Rad AG50W-X8 (200-400 mesh) resin and then rinsed with 15 mL of 0.5
182 mol $L^{-1}$ $HNO_3$ to remove the matrix elements. The K fraction containing ~ 100% of total K was
183 collected with 20 mL 0.5 mol $L^{-1}$ $HNO_3$ and subsequently dried. The same purification process
184 was repeated two to four times to ensure complete matrix removal. The final K solution was
185 redissolved in 2% $HNO_3$ ready for measurement. The total procedural blank for the K isotope
186 analyses was < 30 ng K, which was negligible compared with the concentration of K in the
187 chemically purified solution. Potassium isotopic measurements were performed on the Nu
188 Sapphire CC-MC-ICP-MS (Nu Instruments, Wrexham, UK) using the collision cell (low-energy)
189 path. The hexapole collision cell utilizes He and $H_2$ gas to almost completely remove various Ar-
190 based polyatomic species, so the K isotopic ratios can be measured in the low-resolution mode. An
191 auto-sampler SC-2DX (Elemental Scientific, U.S.A.) was connected to an Apex Omega
192 desolvating nebulizer system (Elemental Scientific, U.S.A.) for sample introduction. One Faraday
193 cup was connected to a pre-amplifier fitted with a $10^{10}$ Ω resistor for collection of $^{39}K^+$ ion beam,
194 while the other two Faraday cups using $10^{11}$ Ω resistors, collected $^{41}K^+$ and mass 40 beams,
195 respectively. Potassium isotopic data are reported in δ notation relative to SRM 3141a, using the
196 sample-standard bracketing technique for instrumental mass fractionation correction (Hu et al.,
197 2018):

This is the peer-reviewed, final accepted version for American Mineralogist, published by the Mineralogical Society of America.
The published version is subject to change. Cite as Authors (Year) Title. American Mineralogist, in press.
DOI: https://doi.org/10.2138/am-2023-9006. http://www.minsocam.org/

$$\delta^{41}\mathrm{K}\,(‰) = \left[\frac{\left(^{41}\mathrm{K}/^{39}\mathrm{K}\right)_{\mathrm{sample}}}{\left(^{41}\mathrm{K}/^{39}\mathrm{K}\right)_{\mathrm{SRM\ 3141a}}} - 1\right] \times 1000$$

198 The K concentration difference between each sample and the standard was controlled to a
199 level below 5%. Each analysis consisted of 1 block of 50 cycles with 4 s integrations. Seven
200 repeated analyses were conducted on each sample solution. Geostandards BCR-2 ($\delta^{41}$K= -0.455 ±
201 0.037‰) and GSR-1 ($\delta^{41}$K = -0.473 ± 0.032‰) that were analyzed during the course of this
202 analysis are consistent with literature values (Chen et al., 2021; Li et al., 2020, 2022; Moynier et
203 al., 2021; Xu et al., 2019). The long-term precision, based on multiple measurements of BCR-2
204 geostandard, was 0.040‰ (2SD) (Li et al., 2022).

205 **RESULTS**

206 **Mineral phase and chemical composition**

207 The XRPD analyses show that, apart from the major K-feldspar phase, most samples
208 occurring as mineral separates still contain some impurities such as albite, quartz, and kaolinite
209 (Table S1 and Figs S1-S11). Some K-feldspars have appreciable $Na_2O$, including the single phase
210 sanidine FHS-1. To avoid confusion, we use the term 'K-feldspar' for bulk K-feldspar samples,
211 and 'K-feldspar phase' and 'albite phase' for the K- and Na-end member components,
212 respectively. The amount of albite phase is in the range of 3.5 - 27.3 wt%, indicating that a routine
213 sample preparation method may have difficulties in separating K-feldspar from albite. The degree
214 of Al/Si order in the studied K-feldspar covers a wide range from 0.22 to 0.94 (1.0 = completely
215 ordered, see details in Table S1).

216 The eleven bulk samples display rather similar chemical compositions (Table 1), and have
217 $K_2O$ contents of 10.3 - 14.2% and $Na_2O$ of 1.00 - 3.85%. They show 2.5% and 1.4% variation for

$SiO_2$ and $Al_2O_3$, respectively, corresponding to a change of Al/Si mole ratio from 0.325 to 0.354. All samples, except FHS-1, have >0.90 mole fraction of K in the K-feldspar phase and >0.90 mole fraction of Na in the albite phase, respectively (Table 2). Therefore, the weights of $K_2O$ in the sample ($K_A$) were mainly derived from the K-feldspar phase (Table 2). To calculate the chemical compositions of the bulk samples, we combined the electron microprobe analysis (EMPA) data (Table 2) with the phase abundance obtained from XRPD (Table S1) and applied theoretical formulas for quartz ($SiO_2$) and kaolinite ($Al_4[Si_4O_{10}](OH)_8$) (The calculated results were supplied in Table S2). We found a strong correlation between the calculated values and the determined ones by XRF for $K_2O$, $Na_2O$, $SiO_2$, $Al_2O_3$, and Al/Si mole ratio (Figs. 1, 2). However, a deviation from the 1:1 diagonal was observed for $Al_2O_3$, indicating a lower content was possibly estimated from the EMPA method, resulting in a lower Al/Si mole ratio for the EMPA analysis relative to XRF (Fig. 2c). Overall, the good consistency between the calculated values and the chemical compositions determined by XRF indicates a relatively high accuracy of both the quantitative phase analysis by the Rietveld method and the method of EMPA.

**K isotopic composition**

The eleven bulk samples have $\delta^{41}K$ values ranging from -0.710 to -0.075‰ (Table 1). The $\Delta^{41}K$ values (the difference between the heaviest and lightest K isotopic composition) for bulk samples from the same lithology and locality are: 0.189‰ for samples TYG-3 and TYG-4 (granite, Chifeng city, Inner Mongolia), 0.296‰ for samples CSY-1, CSY-2, and CSY-3 (syenite porphyry, Chifeng city, Inner Mongolia), and 0.252‰ for samples LS-1 and LS-2 (granitic pegmatite, Lingshou County, Hebei Province). All the porphyry samples have relatively light K isotopes in K-feldspar ($\delta^{41}K$ = -0.710 to -0.220‰), whereas the two pegmatite K-feldspar samples

have relatively heavier compositions ($\delta^{41}K$ = -0.327‰ and -0.075‰).

## DISCUSSION

### Relationship among mineral phase, degree of Al/Si order, and K isotopic composition

The consistency of the degrees of Al/Si order determined from both XRPD (*Z* in Table S1) and Fourier transform infrared spectra (Liu and Zhai, 2021) indicates that the impurities in the mineral separates have negligible impact on determining unit cell parameters of the major K-feldspar phase. The overall degrees of Al/Si order of these studied samples increase in the order of sanidine < orthoclase < microcline (Table S1). The low degree of Al/Si order in sanidine, a high-temperature alkali feldspar, is reflected by its instability in rocks on the surface or shallow levels below the Earth's surface, as well as its transition to orthoclase phase over time (Haldar and Tišljar, 2014). Studies have shown that alkali feldspars with the highest degree of disorder begin to crystallize at about ~1000 °C (Brown and Parsons, 1989; Laves, 1952; Parsons, 2010; Schairer, 1950), whereas the feldspars with high degree of order commonly reach equilibration at temperatures of around 400 °C, which is the inversion temperature of orthoclase into microcline (Brown and Parsons, 1989; Glazner and Johnson, 2013; Kovács Kis et al., 2004; Parsons, 2010; Parsons and Lee, 2009). However, the K-Na exchange reaction can continue at temperatures of <200 °C (Brown and Parsons, 1989; Laves, 1952; Parsons, 2010; Smith and MacKenzie, 1958). A maximum fractionation factor between albite and K-feldspar (microcline) was calculated to be about 0.895 ‰ based on the calculation of Li et al., assuming ~200 °C as the lowest temperature of K isotopic fractionation (Li et al., 2019b). Additionally, Zeng et al. (2019) obtained a larger K isotopic fractionation factor at room temperature. However, taking into account the relative weight of $K_2O$ in the studied samples ($K_A$ in Table 2) and employing the isotopic mixing model (Gray,

1984), the K-feldspar phase of all samples significantly contributes over 98% to the $\delta^{41}K$ value, emphasizing the dominant role of K isotopic behavior within the K-feldspar phase, consistent with its function as the primary K host in these bulk samples.

The low correlation coefficient ($R^2$ = 0.01) between $\delta^{41}K$ and the degree of Al/Si order suggests that the degree of Al/Si order does not significantly affect the K isotopic composition (Fig. 3). Although the K isotopic variation introduced by source heterogeneity (in this context, referring to changes in lithological subtypes or sample localities) cannot be completely ruled out here, the trivial effect of the degree of Al/Si order on the variation of K isotopic composition indicates that crystallization temperature may not be a major factor in controlling K isotopic fractionation in natural K-feldspars.

Preferred orientation, which makes it difficult to obtain high-quality XRPD data for calculating accurate bond length, is significant during sample preparation (Liu et al., 2017; Liu, 2015), and therefore the unit cell parameters of the K-feldspar phase were only calculated by applying the Rietveld method (Table S1). A detailed list of the unit cell parameters is available in Liu and Zhai (2021). The significant linear correlation between the K-O bond length and the unit cell volume of K-feldspar (Fig. 4a) allowed us to calculate the K-O bond length of the K-feldspar phase, using equation 1:

$$d_{K-O} = 0.00308 \times V + 0.7967\ (\text{Å}) \quad (1)$$

Where $d_{K\text{-}O}$ denotes K-O bond length, and $V$ is unit cell volume of K-feldspar phase. The calculated K-O bond lengths were plotted against the corresponding degrees of Al/Si order for the K-feldspar phases (Fig. 4b). The result shows that the correlation between the K-O bond length and the degree of order is negligible, consistent with previously published data (See references in

Table S3).

**Relationship between chemical composition and K isotopic fractionation**

Since the $\delta^{41}K$ values were obtained from a whole bulk sample rather than a single K-feldspar phase, we first investigated the relationship between the $\delta^{41}K$ values and chemical compositions of K-feldspar bulk samples. The $\delta^{41}K$ values and chemical compositions (e.g., $K_2O$, $Na_2O$, and CaO) are negligibly correlated, indicating that the contents of K, Na, and Ca in these samples have little effect on the K isotopic composition (Fig. 5). However, the strong correlations between $\delta^{41}K$ and the contents of Si and Al in the bulk samples are indicated by the high $R^2$ values of 0.79, 0.78, and 0.73 for $\delta^{41}K$ vs. $SiO_2$, $Al_2O_3$, and Al/Si mole ratio, respectively (Fig. 6). The strong correlation of the $\delta^{41}K$ data of the eleven bulk samples in this study vs. the Al/Si ratio, together with eight sets of K-feldspars from China, Norway, and France (Chen et al., 2019; Huang et al., 2023; Kuhnel et al., 2021), indicates a potential dependence of K-feldspar $\delta^{41}K$ on the Al and Si contents. This correlation holds even when accounting for differences in lithology and sample locations. The correlation becomes less pronounced when the $\delta^{41}K$ data are plotted against the Al/Si mole ratio in the K-feldspar phases rather than the bulk samples (Fig. 7); however, the trend still exists (refer to the subsequent discussion).

During the mineral separation process, we found it challenging to completely separate K-feldspar from albite, as previously mentioned. Therefore, it may be a common phenomenon that nominal K-feldspar samples contain some component of an albite phase, as shown in Table S1. The bulk samples in this study have K contents similar to those from the literature (Fig. 7). As a result, it is plausible that the nominal K-feldspar samples from other studies are similarly mixtures of K-feldspar and albite, both of which belong to alkali feldspar. Therefore, the Al/Si-dependent K

306 isotopic composition may be applicable to nominal K-feldspar, i.e., all unaltered, K-dominant
307 alkali feldspar regardless of minor albite inclusions. The diminished correlation using in situ
308 (EPMA) versus bulk (XRF) data shown in Fig. 7 arises from potential errors in the Al/Si ratio of
309 K-feldspar from previously published data. Specifically, this discrepancy may stem from the use
310 of nominal K-feldspar samples for Al/Si ratio, rather than data derived directly from the K-
311 feldspar phase itself. While the K isotopic composition of our studied samples is dominantly
312 influenced by the K-feldspar phase, it is important to acknowledge that the presence of an albite
313 component within the studied sample cannot be entirely ruled out. Furthermore, the observed
314 weaker correlation between $\delta^{41}K$ and Al/Si within the K-feldspar phases, as opposed to the bulk
315 samples, can be partly attributed to the lower precision associated with the determination of Al and
316 Si contents using in situ EMPA in K-feldspar phases, compared to bulk XRF data. This
317 discrepancy arises due to the larger volume of powder used for bulk XRF analysis. Consequently,
318 the enhanced linear correlation observed in the bulk samples, suggests a direct influence of albite
319 on this relationship.

320 Moreover, the trend of Al/Si-dependent $\delta^{41}K$ appears insignificant when the application is
321 extended to plagioclase due to a significant widening of Al/Si mole ratio range (0.185 - 0.466)
322 (Fig. 8a). In contrast to K-feldspar, K content could be a better proxy for constraining the K
323 isotopic composition of plagioclase because its $\delta^{41}K$ value significantly increases with the
324 decreasing K content (Fig. 8b). Considering that the radius of K (1.52 Å) is larger than those of Na
325 (1.16 Å) and Ca (1.14 Å), if they are all coordinated by six O atoms (Shannon, 1976), plagioclase
326 with lower K contents theoretically tend to have shorter K-O bonds, leading to an enrichment of
327 heavy K isotopes (Huang et al., 2023; Kuhnel et al., 2021; Li et al., 2019b; Zeng et al., 2019).

However, the effects of Na or Ca on K isotopic compositions may be relatively small for both K-feldspar and plagioclase, as suggested by the scattered plot of $\delta^{41}K$ vs. Ca/(Ca+Na) (Fig. 8c).

**Mechanism of Al/Si dependence on K isotopic fractionation**

It is important to better understand the relationship between $\delta^{41}K$ and the Al and Si contents of K-feldspar samples. The theoretical expectation of heavy K isotopic enrichment with shorter K-O bond length (Fig. 9a) reasonably agrees with the shortened K-O bond length with increasing Al/Si ratio (Fig. 9b). Even when these three samples (red stars in Fig. 9b) were included, a consistent negative relationship between the Al/Si mole ratio and K-O bond length remained evident, although a more linear regression was obtained when they were excluded. The significant K isotopic variation among these bulk samples suggests K isotopic fractionation is controlled principally by changes in the K-O bond length, which in turn is dictated by contents of Al and Si.

The studied samples from the seven districts of China cover a range in granitic bulk composition, which may have introduced an initial K isotope heterogeneity. The $\delta^{41}K$ values of the two K-feldspar separates from the granite in this study are -0.525‰ and -0.336‰, respectively. These values are heavier relative to the -0.66 to -0.53‰ for the four K-feldspar separates from the Dabie granitoids (Huang et al., 2023), and they also overlap with the -0.79 to -0.47‰ for the seven mineral separates from the Himalayan leucogranites (Huang et al., 2023). Furthermore, the $\delta^{41}K$ values of -0.525‰ and -0.336‰ are close to the K isotopic compositions of two mineral separates from granite sample (-0.46‰ and -0.26‰) (Kuhnel et al., 2021; Xu et al., 2019). The variation in $\delta^{41}K$ values may essentially stem from the K isotopic heterogeneity of magma sources because of the small inherent variations in the crust. Nonetheless, the essential source heterogeneity has not affected the positive correlation between $\delta^{41}K$ and Al/Si ratio

observed for the samples with similar chemical compositions in this study and in the literature. Therefore, the trend may be common for K-feldspar. The chemical composition, such as an increasing Al/Si ratio (Fig. 6c) and a decreasing K content (Fig. 8b) determines the K-O bonding environment, which subsequently dictates K isotopic fractionation (Fig. 9b). For instance, the chemical composition of $Ca_{0.96875}K_{0.03215}Al_{1.96875}Si_{2.03215}O_8$ closely resembles that of the plagioclase endmember $CaAl_2Si_2O_8$, which possesses a theoretical K-O bond length of 2.68 Å (Kuhnel et al., 2021), contrasting significantly with the theoretical K-O bond length of 2.88 Å in microcline (Fig. 10). A large inter-mineral isotopic fractionation of up to 0.863‰ between plagioclase and K-feldspar was observed by Kuhnel et al. (2021). The large inter-mineral fractionation of isotopes should be closely related to the 0.2 Å K-O difference (Huang et al. 2023; Kuhnel et al., 2021). Additionally, the negative correlation observed between K-O bond length and Al/Si mole ratio, as depicted in Fig. 10, aligns with the observed trend in K-feldspar (Fig. 9b).

Previous studies have demonstrated significant K isotopic fractionation during magmatic differentiation, primarily associated with the fractionation of K-rich minerals (Ding et al., 2023; Huang et al., 2023; Su et al., 2023; Wang et al., 2022). The potential impact of inter-mineral K isotopic fractionation on shaping K isotopic behavior is noteworthy. However, it is important to acknowledge that our study lacks $\delta^{41}K$ data from other minerals present in the examined rocks, limiting our ability to directly address questions of inter-mineral fractionation. Despite previous studies demonstrating or theorizing variations in K isotopes among different feldspars (Huang et al., 2023; Kuhnel et al., 2021; Li et al., 2019b; Zeng et al., 2019), the available data from our study reveal only a marginal correlation between $\delta^{41}K$ values and $K_2O$, $Na_2O$, and CaO (Fig. 5), implying that the variation in K isotopes caused by K isotopic fractionation between albite and K-

372 feldspar might not be of significant consequence.

373 **IMPLICATIONS**

374 The K isotopic composition of feldspar is influenced by several factors, such as temperature,
375 the K isotopic composition of the magma in equilibrium, and possible interaction with late-stage
376 fluids or potential effects of surficial/low temperature alteration (Wang et al., 2020, 2021). To
377 assess potential effects of surficial/low temperature alteration, e.g., the extent of chemical
378 weathering, on K isotopic fractionation in the studied bulk samples, we calculated the chemical
379 index of weathering (CIA) values for the studied samples, which range from 50% to 53% (Table
380 1). These values closely resemble those of unaltered granitic rocks (approximately 50%) reported
381 by Ohta and Arai (2007) and Perri (2020). This suggests that the studied bulk samples are very
382 fresh, and the observed variability in K isotopic composition is unlikely to be attributed to
383 weathering processes. Although we cannot control the effects of the source magma, the Al/Si ratio
384 of K-feldspars from different lithologies and locations can be used to constrain the K isotopic
385 composition very well. Recently, studies of Huang et al. (2023) and Wang et al. (2022) revealed
386 large K isotopic fractionation during granitic magmatism. Granitoids with high Si and K have
387 relatively variable Al content (Liu et al., 2010, 2014; Wu et al., 2015). Therefore, to some extent,
388 the variation of Al/Si ratio and $K_2O$ content in feldspar can be attributed to the various geological
389 settings or different stages of magma evolution (Huang et al., 2023). Our study demonstrates that
390 the Al/Si mole ratio can be used as a proxy to constrain the K isotopic composition in K-feldspar
391 in granitic rocks.

392 **DECLARATION OF COMPETING INTEREST**

393 The authors declare that they have no known competing financial interests or personal

relationships that could have appeared to influence the work reported in this paper.

**ACKNOWLEDGMENTS** We would like to thank Dr. Youlian Li for assistance in chemical purification and Dr. Lingli Zhou for critical comments and grammatical correction in improving the quality of this manuscript. Insightful comments from AM Editor Paul Tomascak, Dr. Shi-Chun Huang, and two anonymous reviewers are gratefully acknowledged. This study was financially supported by Second Tibetan Plateau Scientific Expedition and Research Program (STEP) (2019QZKK0802), the Beijing Natural Science Foundation (8202048), and the Experimental Technology Innovation Fund of the Institute of Geology and Geophysics, Chinese Academy of Sciences (Grant No. TEC 202103).

## APPENDIX A. SUPPLEMENTARY MATERIAL

Supplementary data accompanying this article include: Table S1 Parameters obtained from X-ray powder diffraction using the Rietveld method; Table S2 Chemical compositions (wt%) of the bulk samples calculated by combining EMPA and XRPD data; Table S3 Compiled crystal structure data of K-feldspars in Fig. 4. Figures S1-S11 Rietveld fit patterns of all samples.

## REFERENCES

Bish, D. L. (1993) Rietveld refinement of the kaolinite structure at 1.5 K. Clays and Clay Minerals, 41, 738-744.

Brown, W. L. and Parsons, I. (1989) Alkali feldspars–ordering rates, phase-transformations and behavior diagrams for igneous rocks. Mineralogical Magazine, 53, 25-42.

Brown, W. L. and Parsons, I. (1994) Feldspars in Igneous Rocks. In I. Parsons, Eds., Feldspars and their Reactions, p. 449-499. Springer Netherlands, Dordrecht.

Černý, P. (1994) Evolution of Feldspars in Granitic Pegmatites. In I. Parsons, Eds., Feldspars and their Reactions, p. 501-540. Springer Netherlands, Dordrecht.

Chen, H., Saunders, N. J., Jerram, M. and Halliday, A. N. (2021) High-precision potassium isotopic

measurements by collision cell equipped MC-ICPMS. Chemical Geology, 578, 120281.

Chen, H., Tian, Z., Tuller-Ross, B., Korotev, R. L. and Wang, K. (2019) High-precision potassium isotopic analysis by MC-ICP-MS: an inter-laboratory comparison and refined K atomic weight. Journal of Analytical Atomic Spectrometry, 34, 160-171.

Colville, A. A. and Ribbe, P. H. (1968) The crystal structure of an adularia and a refinement of the structure of orthoclase. American Mineralogist, 53, 25-37.

Cui, M.L., Zhang, B.L., Peng, P., Zhang, L.C., Shen, X.L., Guo, Z.H., Huang, X.F. (2010) Zircon/baddeleyite U-Pb dating for the Paleo-proterozoic intermediate-acid intrusive rocks in Xiaoshan Mountains, west of Henan Province and their contraints on the age of the Xiong'er Volcanic Province. Acta Petrologica Sinica, 26 (5), 1541–1549 (in Chinese with English abstract).

Dal Negro, A., De Pieri, R., Quareni, S. and Taylor, W. H. (1978) The crystal structures of nine K feldspars from the Adamello Massif (Northern Italy). Acta Crystallographica, Section B: Structural Crystallography and Crystal Chemistry, 34, 2699-2707.

d'Amour, H., Denner, W. and Schulz, H. (1979) Structure determination of α-quartz up to $68 \times 10^8$ Pa. Acta Crystallographica, Section B: Structural Crystallography and Crystal Chemistry, 35, 550-555.

Ding, Z.Y., Liu, S.K., Su, B.X., Li, W.J., Bai, Y., Pan, Q.Q., Hu, F.Y. and Pang, K.N. (2023) Potassium isotope fractionation during granite differentiation and implications for crustal K isotope heterogeneity. Lithos, 448-449, 107176.

Faye, G. and Sutarno, R. (1976) Certified compositional reference materials for the earth sciences. The Canadian Mineralogist, 14, 164-171.

Gering, E. (1985) Silizium/Aluminium-Ordnung und Kristallperfektion von Sanidinen. von der Fakultät für Physik der Universität Karlsruhe (TH) genehmigte Dissertation, Bericht, 3984, 1–97.

Glazner, A. F. and Johnson, B. R. (2013) Late crystallization of K-feldspar and the paradox of megacrystic granites. Contributions to Mineralogy and Petrology, 166, 777-799.

Gonzalez, C. A. (2013) Standard Reference Material 70b. NIST report.

Govindaraju, K. (1984) Report (1973–1984) on two ANRT geochemical reference samples: Granite GS-N and Potash Feldspar FK-N. Geostandards Newsletter, 8, 173-206.

Gray, C. M. (1984) An isotopic mixing model for the origin of granitic rocks in southeastern Australia. Earth And Planetary Science Letters, 70, 47-60.

Guo, L.X. (2019) Study on the Sn metallogenesis in southern part of Da Hinggan Mountains: constraints from Weilasituo and Xiaohaiqing Sn-polymetallic deposits, 96-101 p. Ph. D. thesis, University of Chinese Academy of Sciences, Beijing (in Chinese with English abstract).

Haldar, S. K. and Tišljar, J. (2014) Chapter 2 - Basic Mineralogy. In S. K. Haldar and J. Tišljar, Eds., Introduction to Mineralogy and Petrology, p. 39-79. Elsevier, Oxford.

Hellmann, R., Zhai, Y. Y., Robin, E., Findling, N., Mayanna, S., Wirth, R., Schreiber, A., Cabié, M., Zeng, Q. D., Liu, S. K. and Liu, J. M. (2021) The hydrothermal alkaline alteration of potassium feldspar: A nanometer-scale investigation of the orthoclase interface. Chemical Geology, 569, 120133.

Hollabaugh, C. L. (2007) Modification of Goldschmidt's geochemical classification of the elements to include arsenic, mercury, and lead as biophile elements. Developments in environmental science 5, 9-31.

Hu, Y., Chen, X. Y., Xu, Y. K. and Teng, F. Z. (2018) High-precision analysis of potassium isotopes by HR-MC-ICPMS. Chemical Geology, 493, 100-108.

Hu Y., Teng F. Z., Helz R. T. and Chauvel C. (2021) Potassium isotope fractionation during magmatic differentiation and the composition of the mantle. Journal of Geophysical Research-Solid Earth, 126, e2020JB021543.

Huang, T. Y., Teng, F. Z., Wang, Z. Z., He, Y. S., Liu, Z. C. and Wu, F. Y. (2023) Potassium isotope fractionation during granitic magmatic differentiation: mineral-pair perspectives. Geochimica et Cosmochimica Acta, 343, 196-211 .

Kovács Kis, V., Horvat, M. and Dodony, I. (2004) Microstructures in two alkali feldspar megacrysts from the Papuk Mt., Croatia. Geologia Croatica, 57, 149-158.

Kuhnel, W. W., Jacobsen, S. B., Li, Y., Ku, Y., Petaev, M. I., Huang, S., Wu, Z. and Wang, K. (2021) High-temperature inter-mineral potassium isotope fractionation: Implications for K–Ca–Ar chronology. ACS Earth and Space Chemistry, 5, 2740-2754.

Larson, A. C. and Von Dreele, R. B. (2004) General Structure Analysis System (GSAS). Los Alamos National Laboratory Report LAUR, 86-748.

Laves, F. (1952) Phase relations of the alkali feldspars: I. Introductory remarks. The Journal of Geology, 60, 436-450.

Li, W. J., Cui, M. M., Pan, Q. Q., Wang, J., Liu, S. K., Yuan, M., Su, B. X., Zhao, Y., Teng, F. Z. and Han, G. L. (2022) High-precision potassium isotope analysis using the Nu Sapphire collision cell (CC)-MC-ICP-MS. Science China Earth Sciences, 65, 1510-1521.

Li, W. Q., Beard, B. L. and Li, S. L. (2016) Precise measurement of stable potassium isotope ratios using a single focusing collision cell multi-collector ICP-MS. Journal of Analytical Atomic Spectrometry, 31, 1023-1029.

Li, X. Q., Han, G. L., Zhang, Q. and Miao, Z. (2020) An optimal separation method for high-precision K isotope analysis by using MC-ICP-MS with a dummy bucket. Journal of Analytical Atomic Spectrometry, 35, 1330-1339.

Li, Y. H., Wang, W. Z., Wu, Z. Q. and Huang, S. C. (2019a) First-principles investigation of equilibrium K isotope fractionation among K-bearing minerals. Geochimica et Cosmochimica Acta, 264, 30-42.

Li, Y. H., Wang, W. Z., Huang, S. C., Wang, K. and Wu, Z. Q. (2019b) First-principles investigation of the concentration effect on equilibrium fractionation of K isotopes in feldspars. Geochimica et Cosmochimica Acta, 245, 374-384.

Liu, S. A., Teng, F. Z., He, Y., Ke, S. and Li, S. (2010) Investigation of magnesium isotope fractionation during granite differentiation: Implication for Mg isotopic composition of the continental crust. Earth And Planetary Science Letters, 297, 646-654.

Liu, S. K. (2015) Rietveld structure refinement of microcline. European Journal of Mineralogy, 27, 501-510.

Liu, S. K., Li, H.. and Liu, J. M. (2017) An updated model of Rietveld structure refinement of Na/K-feldspar. Periodico Di Mineralogia, 86, 75-85.

Liu, S. K. and Zhai, Y. Y. (2021) Degree of Al-Si order in K-feldspar and its effect on K-feldspar's dissolution. Periodico di Mineralogia, 90, 359-369.

Liu, Z. C., Wu, F. Y., Ji, W. Q., Wang, J. G., Liu, C. Z. (2014) Petrogenesis of the Ramba leucogranite in the Tethyan Himalaya and constraints on the channel flow model. Lithos, 208–209, 118-136.

Meng, S., Yan, C., Lai, Y., Shu, Q. H. and Sun, Y. (2013) Study on the mineralization chronology and

characteristics of mineralization fluid from the Chehugou porphyry Mo-Cu deposit, Inner Mongolia. Acta Petrologica Sinica, 29, 255-269 (in Chinese with English abstract).

Morgan, L. E., Ramos, D. P. S., Davidheiser-Kroll, B., Faithfull, J., Lloyd, N. S., Ellam, R. M. and Higgins, J. A. (2018) High-precision $^{41}K/^{39}K$ measurements by MC-ICP-MS indicate terrestrial variability of $\delta^{41}K$. Journal of Analytical Atomic Spectrometry, 33, 175-186.

Moynier, F., Hu, Y., Wang, K., Zhao, Y., Gerard, Y., Deng, Z. B., Moureau, J., Li, W. Q., Simon, J. I. and Teng, F. Z. (2021) Potassium isotopic composition of various samples using a dual-path collision cell-capable multiple-collector inductively coupled plasma mass spectrometer, Nu instruments Sapphire. Chemical Geology, 571, 120144.

Ohta, T. and Arai, H. (2007) Statistical empirical index of chemical weathering in igneous rocks: A new tool for evaluating the degree of weathering. Chemical Geology, 240, 280-297.

Oneil, J. R. (1977) Stable isotopes in mineralogy. Physics and Chemistry of Minerals, 2, 105-123.

Oneil, J. R. (1986) Theoretical and experimental aspects of isotopic fractionation. Reviews in Mineralogy & Geochemistry, 16, 1-40.

Parsons, I. (2010) Feldspars defined and described: a pair of posters published by the Mineralogical Society. Sources and supporting information. Mineralogical Magazine, 74, 529-551.

Parsons, I. and Lee, M. (2009) Mutual replacement reactions in alkali feldspars I: microtextures and mechanisms. Contributions to Mineralogy and Petrology, 157, 641-661.

Perri, F. (2020) Chemical weathering of crystalline rocks in contrasting climatic conditions using geochemical proxies: An overview. Palaeogeography, Palaeoclimatology, Palaeoecology, 556, 109873.

Reed, W. (1990) Standard reference material 99a. NIST report.

Schairer, J. t. (1950) The alkali-feldspar join in the system $NaAlSiO_4$-$KAlSiO_4$-$SiO_2$. The Journal of Geology, 58, 512-517.

Schauble, E. A. (2004) Applying stable isotope fractionation theory to new systems. Reviews in Mineralogy & Geochemistry, 55, 65-111.

Shannon, R. D. (1976) Revised effective ionic radii and systematic studies of interatomic distances in halides and chalcogenides. Acta crystallographica section A: crystal physics, diffraction, theoretical and general crystallography, 32, 751-767.

Smith, J. and MacKenzie, W. (1958) The alkali feldspars: IV. The cooling history of high-temperature sodium-rich feldspars. American Mineralogist, 43, 872-889.

Smith, J. V. and Brown, W. L. (1988a) Introduction. In Feldspar Minerals: Volume 1 Crystal Structures, Physical, Chemical, and Microtextural Properties, p. 3-20. Springer Berlin Heidelberg, Berlin, Heidelberg..

Smith, J. V. and Brown, W. L. (1988b) Order-Disorder. In Feldspar Minerals: Volume 1 Crystal Structures, Physical, Chemical, and Microtextural Properties, p. 33-54.. Springer Berlin Heidelberg, Berlin, Heidelberg.

Stosch, H. G. (1998) Elements: Lithophile. In Geochemistry, p. 214-215. Springer Netherlands, Dordrecht.

Su, B.X., Pan, Q.Q., Bai, Y., Li, W.J., Cui, M.M., Pang, K.N. (2023) Potassium isotope fractionation during silicate-carbonatite melt immiscibility and phlogopite fractional crystallization. American Mineralogist, https://doi.org/10.2138/am-2022-8898.

Toby, B. H. (2001) EXPGUI, a graphical user interface for GSAS. Journal of Applied Crystallography, 34, 210-213.

Urey, H. C. (1947) The thermodynamic properties of isotopic substances. Journal of the Chemical Society (Resumed), 562-581.

Vernon, R. H. and Paterson, S. R. (2008) How late are K-feldspar megacrysts in granites? Lithos, 104, 327-336.

Wang, K. and Jacobsen, S. B. (2016) An estimate of the Bulk Silicate Earth potassium isotopic composition based on MC-ICPMS measurements of basalts. Geochimica et Cosmochimica Acta, 178, 223-232.

Wang, K., Li, W. Q. and Li, S. L. (2020) Potassium stable isotope geochemistry and cosmochemistry. Earth Science Frontiers, 27, 1-19.

Wang, K., Li, W. Q., Li, S. L., Tian, Z., Koefoed, P. and Zheng, X. Y. (2021) Geochemistry and cosmochemistry of potassium stable isotopes. Geochemistry, 81, 125786.

Wang, Z. Z., Teng, F. Z., Wu, F. Y., Liu, Z. C., Liu, X. C., Liu, S. A. and Huang, T. Y. (2022) Extensive crystal fractionation of high-silica magmas revealed by K isotopes. Science Advances, 8, eabo4492.

Webber, G. (1961) Report of nonmetallic standards committee Canadian association for applied spectroscopy. Applied Spectroscopy, 15, 159-161.

Wenk, H.R. and Kroll, H. (1984) Analysis of P-1, I-1 and C-1 plagioclase structures. Bulletin de Mineralogie, 107, 467-487.

Wu, F. Y., Liu, Z. C., Liu, X. C., Ji, W. Q. (2015) Himalayan leucogranite: Petrogenesis and implications to orogenesis and plateau uplift. Acta Petrologica Sinica, 31, 1-36 (in Chinese with English abstract).

Wu, G., Li, X. Z., Xu, L. Q., Wang, G. R., Liu, J., Zhang, T., Quan, Z. X., Wu, H., Li, T. G., Zeng, Q. T. and Chen, Y. C. (2017) Age, geochemistry, and Sr-Nd-Hf-Pb isotopes of the Caosiyao porphyry Mo deposit in Inner Mongolia, China. Ore Geology Reviews, 81, 706-727.

Wu, Z. H., Ye, P. S., Hu, D. G., Zhang, W. and Zhou, C. J. (2007) U-Pb isotopic dating of zircons from porphyry granite of the Fenghuoshan mts., northern tibetan plateau and its geological significance. Geoscience 21, 435-442 (in Chinese with English abstract).

Xu, Y. K., Hu, Y., Chen, X. Y., Huang, T. Y., Sletten, R. S., Zhu, D. and Teng, F. Z. (2019) Potassium isotopic compositions of international geological reference materials. Chemical Geology, 513, 101-107.

Yuan, G. H., Cao, Y. C., Schulz, H. M., Hao, F., Gluyas, J., Liu, K. Y., Yang, T., Wang, Y. Z., Xi, K. L. and Li, F. L. (2019) A review of feldspar alteration and its geological significance in sedimentary basins: From shallow aquifers to deep hydrocarbon reservoirs. Earth-Science Reviews, 191, 114-140.

Zeng, H., Rozsa, V. F., Nie, N. X., Zhang, Z., Pham, T. A., Galli, G. and Dauphas, N. (2019) Ab initio calculation of equilibrium isotopic fractionations of potassium and rubidium in minerals and water. ACS Earth and Space Chemistry, 3, 2601-2612.

Zhai, Y. Y,, Hellmann, R., Campos, A., Findling, N., Mayanna, S., Wirth, R., Schreiber, A., Cabié, M., Zeng, Q. D., Liu, S. K. and Liu, J. M. (2021) Fertilizer derived from alkaline hydrothermal alteration of K-feldspar: A micrometer to nanometer-scale investigation of K in secondary reaction products and the feldspar interface. Applied Geochemistry, 126, 104828.

Zhang, T. F., Guo, S., Xin, H. T., Zhang, Y., He, P., Liu, W. G., Zhang, K., Liu, C. B., Wang, K. X., Zhang, C. (2019) Petrogenesis and magmatic evolution of highly fractionated granite and their constraints on Sn-(Li-Rb-Nb-Ta) mineralization in the Weilasituo Deposit, Inner Mongolia,

Southern Great Xing'an Range. Earth Science, 44 (1), 248–257 (in Chinese with English abstract).

**Figure captions:**

**Fig. 1.** Plots of $K_2O$ (wt%), $Na_2O$ (wt%), and CaO (wt%) obtained from XRF vs. those calculated by combining EMPA and XRPD data (see details in the main text, and EMPA represents the calculated values in the abscissa). Dashed line is 1:1 relationship, solid line is linear regression of data with 95% confidence interval in grey shaded region. Same system is used in remaining figures.

**Fig. 2.** Plots of $SiO_2$ (wt%), $Al_2O_3$ (wt%), and Al/Si mole ratio obtained from XRF vs. those calculated by combining EMPA and XRPD data (see details in the main text, and EMPA represents the calculated values in the abscissa).

**Fig. 3.** $\delta^{41}K$ vs. degree of Al/Si order of the studied eleven K-feldspar bulk samples (refer to the text for how Al/Si order is quantified).

**Fig. 4.** K-O bond length vs. (a) unit cell volume and (b) Al/Si order degree, showing linear fit for K-feldspars. The K-O bond lengths were calculated from equation 1 in the text. Data compiled from the literature and this study. See Supplementary Table S3 for details of literature data.

**Fig. 5.** Plots of $\delta^{41}K$ vs. (a) $K_2O$, (b) $Na_2O$, and (c) CaO for the K-feldspar bulk samples.

**Fig. 6.** Plots of $\delta^{41}K$ vs. (a) $SiO_2$, (b) $Al_2O_3$, and (c) Al/Si mole ratio for the K-feldspar bulk samples in this study and from the literature.

**Fig. 7.** Plots of $\delta^{41}K$ vs. Al/Si mole ratio. The data for the studied samples includes solid circles (bulk samples) and open circles (individual K-feldspar phases). The Al/Si more ratios of bulk samples (solid circles) can be found in Table 1, while the individual Al/Si ratios for K-feldspar phases (open circles) are listed in Table 2.

**Fig. 8.** Plots of $\delta^{41}K$ vs. (a) Al/Si mole ratio, (b) K content and (c) Ca/(Ca+Na) mole ratio for K-feldspars analyzed in this study and the literature (filled symbol denotes K-feldspar, and hollow one denotes plagioclase). K content was calculated based on the total moles (up to 1) of Na, K, and Ca in feldspar. The literature data include five sets of feldspar standards and thirty-five sets of feldspar samples. Sources of K isotopic compositions of the feldspar standards are: FK-N (K-feldspar) and NIST SRM 99a (soda feldspar) (Chen et al., 2019), syenites SY-1 and SY-2 (plagioclase) (Xu et al., 2019), and NIST SRM 70b (potassium feldspar) (Morgan et al., 2018). Their major element compositions are from: FK-N (Govindaraju, 1984), NIST SRM 99a (Reed, 1990), SY-1 (Webber G., 1961), SY-2 (Faye and Sutarno, 1976), and NIST SRM 70b (Gonzalez, 2013). K isotopic compositions and major element data of feldspar samples from Kuhnel et al.

(2021) and Huang et al. (2023).

**Fig. 9.** Correlation diagrams of (a) $\delta^{41}K$ vs. K-O bond length and (b)Al/Si mole ratio vs. K-O bond length of K-feldspar phases. To highlight a more pronounced trend observed among the samples, three samples (red stars) were deliberately excluded from the linear regression.

**Fig. 10.** Plot of theoretical K-O bond length vs. Al/Si mole ratio from published feldspar data.

This is the peer-reviewed, final accepted version for American Mineralogist, published by the Mineralogical Society of America.
The published version is subject to change. Cite as Authors (Year) Title. American Mineralogist, in press.
DOI: https://doi.org/10.2138/am-2023-9006. http://www.minsocam.org/

667 **Table 1.** Elemental (wt%) and K isotopic (‰) compositions of K-feldspar samples[1]

| Sample | $SiO_2$ | $TiO_2$ | $Al_2O_3$ | $TFe_2O_3$[2] | MnO | MgO | CaO | $Na_2O$ | $K_2O$ | $P_2O_5$ | LOI[3] | Al/Si[4] | CIA (%)[5] | $\delta^{41}K$ | 2SD | 95%c.i. (‰) | N[6] |
|---|---|---|---|---|---|---|---|---|---|---|---|---|---|---|---|---|---|
| FHS-1 | 64.8 | 0.16 | 19.5 | 0.23 | 0.00 | 0.04 | 0.18 | 3.85 | 10.3 | 0.01 | 0.24 | 0.300 | 52 | -0.222 | 0.062 | 0.029 | 7 |
| CSY-1 | 66.0 | 0.02 | 18.4 | 0.22 | 0.01 | 0.05 | 0.22 | 2.96 | 11.5 | 0.01 | 0.52 | 0.279 | 51 | -0.414 | 0.057 | 0.026 | 7 |
| CSY-2 | 66.0 | 0.03 | 18.3 | 0.21 | 0.00 | 0.08 | 0.14 | 1.00 | 13.3 | 0.02 | 0.82 | 0.277 | 53 | -0.520 | 0.035 | 0.016 | 7 |
| CSY-3 | 65.6 | 0.01 | 18.1 | 0.42 | 0.01 | 0.04 | 0.13 | 1.73 | 13.5 | 0.01 | 0.54 | 0.276 | 51 | -0.710 | 0.089 | 0.041 | 7 |
| CHG-12 | 66.2 | 0.03 | 18.4 | 0.22 | 0.00 | 0.13 | 0.23 | 2.50 | 11.4 | 0.01 | 0.79 | 0.277 | 52 | -0.604 | 0.041 | 0.019 | 7 |
| SX-1 | 64.9 | 0.10 | 18.3 | 0.78 | 0.00 | 0.07 | 0.05 | 1.37 | 14.2 | 0.01 | 0.36 | 0.282 | 51 | -0.452 | 0.062 | 0.029 | 7 |
| LS-1 | 65.0 | 0.06 | 19.0 | 0.05 | 0.00 | 0.02 | 0.07 | 2.45 | 12.8 | 0.01 | 0.20 | 0.291 | 51 | -0.327 | 0.047 | 0.022 | 7 |
| LS-2 | 63.9 | 0.09 | 19.2 | 0.05 | 0.00 | 0.06 | 0.13 | 2.02 | 13.1 | 0.01 | 0.46 | 0.300 | 52 | -0.075 | 0.043 | 0.020 | 7 |
| WLST-1 | 66.0 | 0.01 | 18.3 | 0.04 | 0.00 | 0.02 | 0.01 | 2.22 | 13.1 | 0.01 | 0.08 | 0.277 | 51 | -0.666 | 0.052 | 0.024 | 7 |
| TYG-3 | 66.4 | 0.01 | 18.6 | 0.12 | 0.00 | 0.04 | 0.19 | 3.59 | 11.2 | 0.01 | 0.22 | 0.280 | 50 | -0.525 | 0.061 | 0.028 | 7 |
| Duplicate[7] | | | | | | | | | | | | | | -0.534 | 0.051 | 0.023 | 7 |
| TYG-4 | 65.4 | 0.02 | 18.7 | 0.14 | 0.00 | 0.05 | 0.12 | 2.13 | 13.3 | 0.02 | 0.22 | 0.286 | 51 | -0.336 | 0.063 | 0.029 | 7 |

668 **Note:** 1. All K isotopic compositions were determined in this study, and elemental compositions analyzed using X-ray fluorescence spectrum are from
669 literature: chemical compositions of samples FSH-1, SX-1, LS-1, LS-2, TYG-3, and TYG-4 are from Zhai et al. (2021), and samples CSY-1, CSY-2, CSY-3,
670 CHG-12, and WLST-1 are from Hellmann et al. (2021). 2. total iron oxide. 3. LOI: loss on ignition. 4. The Al/Si mole ratio was obtained by calculating the
671 ratio of the moles of aluminum to silicon. 5. CIA=$\{x(Al_2O_3)/[x(Al_2O_3)+x(CaO^*)+x(Na_2O)+x(K_2O)]\}\times100$, in which $CaO^*$ denotes CaO proportion derived
672 from silicate minerals. 6. number of repeated K isotope analyses. 7. Duplicate: during the process of K isotope analysis, repeat analyses were conducted on
673 the same purified sample solution during different analytical sessions.
674
675
676
677
678
679

This is the peer-reviewed, final accepted version for American Mineralogist, published by the Mineralogical Society of America.
The published version is subject to change. Cite as Authors (Year) Title. American Mineralogist, in press.
DOI: https://doi.org/10.2138/am-2023-9006. http://www.minsocam.org/

680
681
682 **Table 2.** Measured chemical compositions of K-feldspar and albite phases by EMPA

| Sample | wt% | | | | | | | | | | | | mole | | | | $K_A$[2] |
|---|---|---|---|---|---|---|---|---|---|---|---|---|---|---|---|---|---|
| | $SiO_2$ | $TiO_2$ | $Al_2O_3$ | FeO | MnO | MgO | CaO | $Na_2O$ | $K_2O$ | $Cr_2O_3$ | NiO | Total | K | Na | Ca | Al/Si[1] | |
| K-feldspar phase | | | | | | | | | | | | | | | | | |
| FHS-1 | 64.47 | 0.04 | 18.70 | 0.18 | 0.00 | 0.01 | 0.08 | 3.80 | 11.10 | 0.01 | 0.02 | 98.42 | 0.66 | 0.34 | 0.00 | 0.342 | 1.00 |
| CSY-1 | 64.34 | 0.04 | 17.85 | 0.12 | 0.01 | 0.01 | 0.06 | 0.88 | 16.23 | 0.00 | 0.01 | 99.56 | 0.92 | 0.08 | 0.00 | 0.327 | 0.98 |
| CSY-2 | 64.13 | 0.03 | 18.03 | 0.07 | 0.01 | 0.01 | 0.03 | 1.00 | 15.97 | 0.00 | 0.02 | 99.32 | 0.91 | 0.09 | 0.00 | 0.331 | 1.00 |
| CSY-3 | 64.53 | 0.01 | 18.06 | 0.09 | 0.00 | 0.01 | 0.04 | 1.01 | 16.17 | 0.01 | 0.01 | 99.94 | 0.91 | 0.09 | 0.00 | 0.330 | 1.00 |
| CHG-12 | 64.42 | 0.03 | 18.02 | 0.09 | 0.01 | 0.01 | 0.03 | 1.21 | 15.65 | 0.01 | 0.00 | 99.46 | 0.89 | 0.11 | 0.00 | 0.330 | 0.99 |
| SX-1 | 64.66 | 0.02 | 17.48 | 0.61 | 0.01 | 0.01 | 0.01 | 0.75 | 16.44 | 0.00 | 0.01 | 100.00 | 0.94 | 0.07 | 0.00 | 0.319 | 1.00 |
| LS-1 | 64.46 | 0.02 | 18.43 | 0.02 | 0.01 | 0.01 | 0.01 | 0.92 | 16.10 | 0.01 | 0.00 | 100.02 | 0.92 | 0.08 | 0.00 | 0.337 | 1.00 |
| LS-2 | 63.94 | 0.02 | 18.02 | 0.05 | 0.01 | 0.02 | 0.03 | 0.85 | 16.16 | 0.01 | 0.01 | 99.11 | 0.93 | 0.07 | 0.00 | 0.332 | 1.00 |
| WLST-1 | 65.00 | 0.02 | 17.67 | 0.04 | 0.02 | 0.00 | 0.01 | 0.43 | 17.19 | 0.00 | 0.00 | 100.37 | 0.96 | 0.04 | 0.00 | 0.320 | 1.00 |
| TYG-3 | 64.84 | 0.01 | 17.44 | 0.07 | 0.01 | 0.02 | 0.03 | 0.77 | 16.64 | 0.01 | 0.00 | 99.85 | 0.93 | 0.07 | 0.00 | 0.317 | 1.00 |
| TYG-4 | 64.47 | 0.03 | 17.93 | 0.04 | 0.01 | 0.00 | 0.03 | 0.90 | 16.57 | 0.01 | 0.01 | 99.98 | 0.92 | 0.08 | 0.00 | 0.328 | 0.99 |
| Albite phase | | | | | | | | | | | | | | | | | |
| CSY-1 | 67.78 | 0.02 | 20.03 | 0.11 | 0.01 | 0.01 | 0.57 | 9.87 | 1.14 | 0.00 | 0.02 | 99.56 | 0.90 | 0.07 | 0.03 | 0.348 | |
| CSY-3 | 68.22 | 0.01 | 19.23 | 0.06 | 0.00 | 0.01 | 0.28 | 10.72 | 0.33 | 0.01 | 0.00 | 98.87 | 0.97 | 0.02 | 0.01 | 0.332 | |
| CHG-12 | 66.98 | 0.02 | 19.88 | 0.11 | 0.02 | 0.04 | 0.74 | 9.96 | 0.74 | 0.00 | 0.01 | 98.49 | 0.92 | 0.04 | 0.04 | 0.350 | |
| SX-1 | 67.95 | 0.01 | 19.04 | 0.52 | 0.02 | 0.01 | 0.02 | 10.87 | 0.31 | 0.00 | 0.01 | 98.76 | 0.98 | 0.02 | 0.00 | 0.330 | |
| LS-1 | 68.38 | 0.01 | 20.04 | 0.03 | 0.01 | 0.01 | 0.44 | 10.15 | 0.22 | 0.00 | 0.00 | 99.30 | 0.96 | 0.01 | 0.02 | 0.345 | |
| LS-2 | 68.02 | 0.02 | 19.72 | 0.04 | 0.02 | 0.00 | 0.43 | 10.93 | 0.29 | 0.01 | 0.00 | 99.48 | 0.96 | 0.02 | 0.02 | 0.342 | |
| WLST-1 | 69.27 | 0.02 | 19.17 | 0.02 | 0.01 | 0.00 | 0.01 | 10.82 | 0.25 | 0.01 | 0.00 | 99.57 | 0.98 | 0.02 | 0.00 | 0.326 | |
| TYG-3 | 67.91 | 0.01 | 19.65 | 0.06 | 0.01 | 0.05 | 0.94 | 10.62 | 0.21 | 0.01 | 0.00 | 99.47 | 0.94 | 0.01 | 0.05 | 0.341 | |
| TYG-4 | 66.88 | 0.01 | 20.20 | 0.18 | 0.00 | 0.06 | 0.89 | 10.35 | 0.63 | 0.01 | 0.01 | 99.22 | 0.92 | 0.04 | 0.04 | 0.356 | |

This is the peer-reviewed, final accepted version for American Mineralogist, published by the Mineralogical Society of America.
The published version is subject to change. Cite as Authors (Year) Title. American Mineralogist, in press.
DOI: https://doi.org/10.2138/am-2023-9006. http://www.minsocam.org/

683 Note: 1. The method used to calculate the Al/Si mole ratio is the same as the one presented in Table 1. However, it is important to note that in Table 2, the
684 Al/Si ratio represents values for the K-feldspar phase and the albite phase, whereas in Table 1, it corresponds to the bulk samples. 2. $K_A$ is the relative
685 contribution of the $K_2O$ content of K-feldspar phase to the sample based on the equation presented by Kuhnel et al. (2021), i.e.,
686 $K_A = \frac{K_2O^1 \times w_{K-feldspar}}{K_2O^1 \times w_{K-feldspar} + K_2O^2 \times w_{albite}}$, in which $K_2O^1$ denotes the $K_2O$ (wt%) content in the K-feldspar phase, and $K_2O^2$ denotes the $K_2O$ (wt%) content in the
687 albite phase.

This is the peer-reviewed, final accepted version for American Mineralogist, published by the Mineralogical Society of America.
The published version is subject to change. Cite as Authors (Year) Title. American Mineralogist, in press.
DOI: https://doi.org/10.2138/am-2023-9006. http://www.minsocam.org/

**Fig. 1**

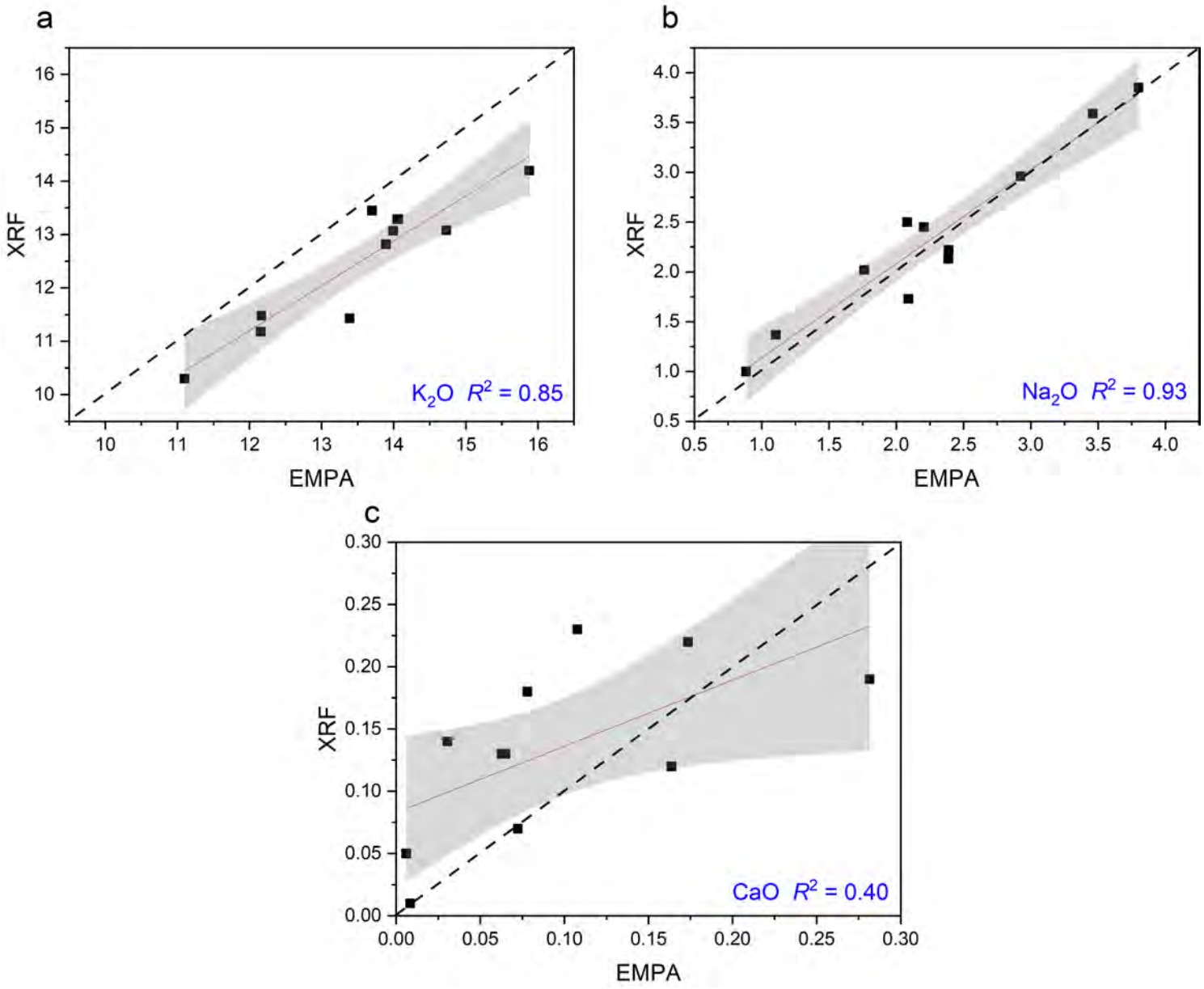

This is the peer-reviewed, final accepted version for American Mineralogist, published by the Mineralogical Society of America.
The published version is subject to change. Cite as Authors (Year) Title. American Mineralogist, in press.
DOI: https://doi.org/10.2138/am-2023-9006. http://www.minsocam.org/

**Fig. 2**

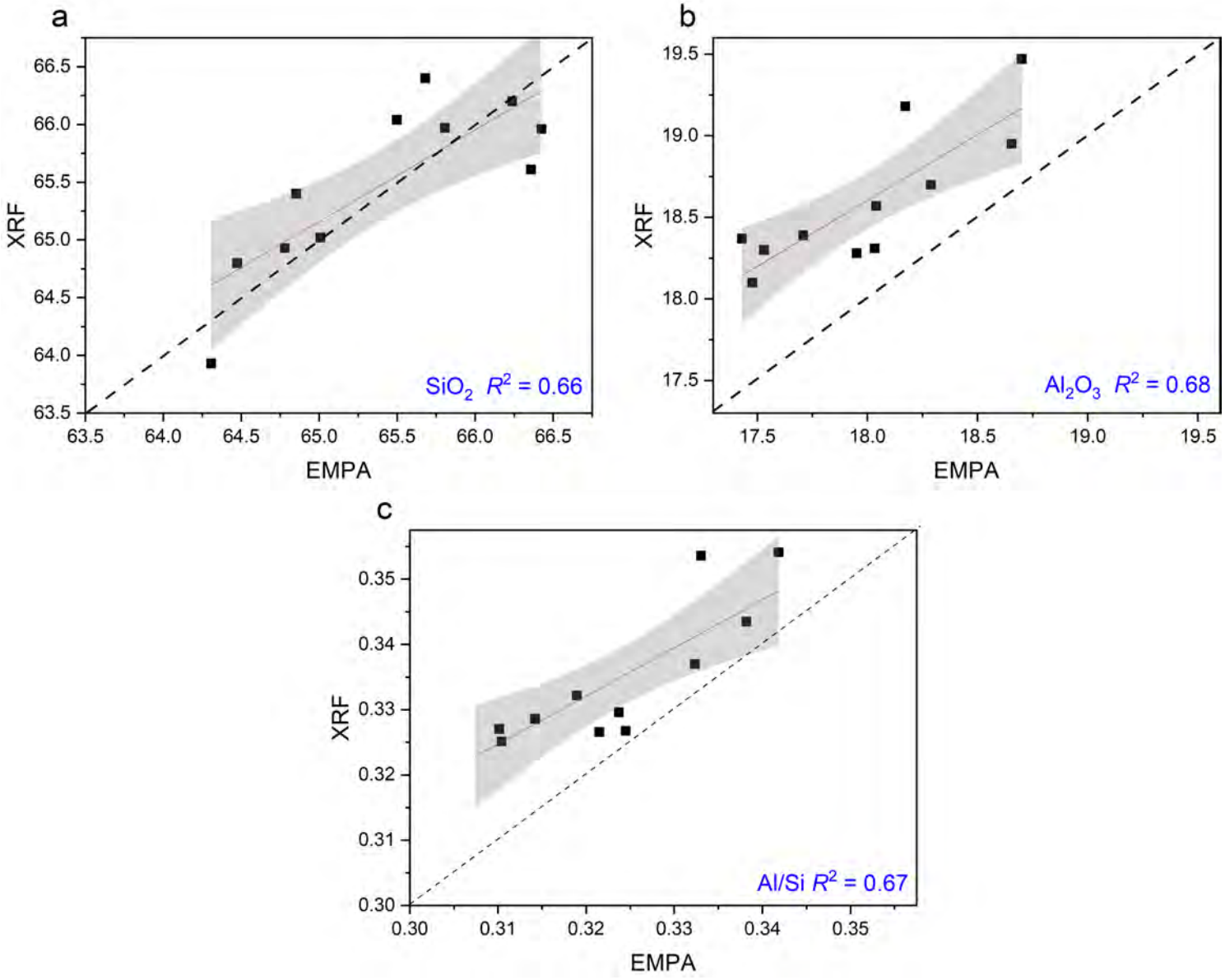

This is the peer-reviewed, final accepted version for American Mineralogist, published by the Mineralogical Society of America.
The published version is subject to change. Cite as Authors (Year) Title. American Mineralogist, in press.
DOI: https://doi.org/10.2138/am-2023-9006. http://www.minsocam.org/

**Fig. 3**

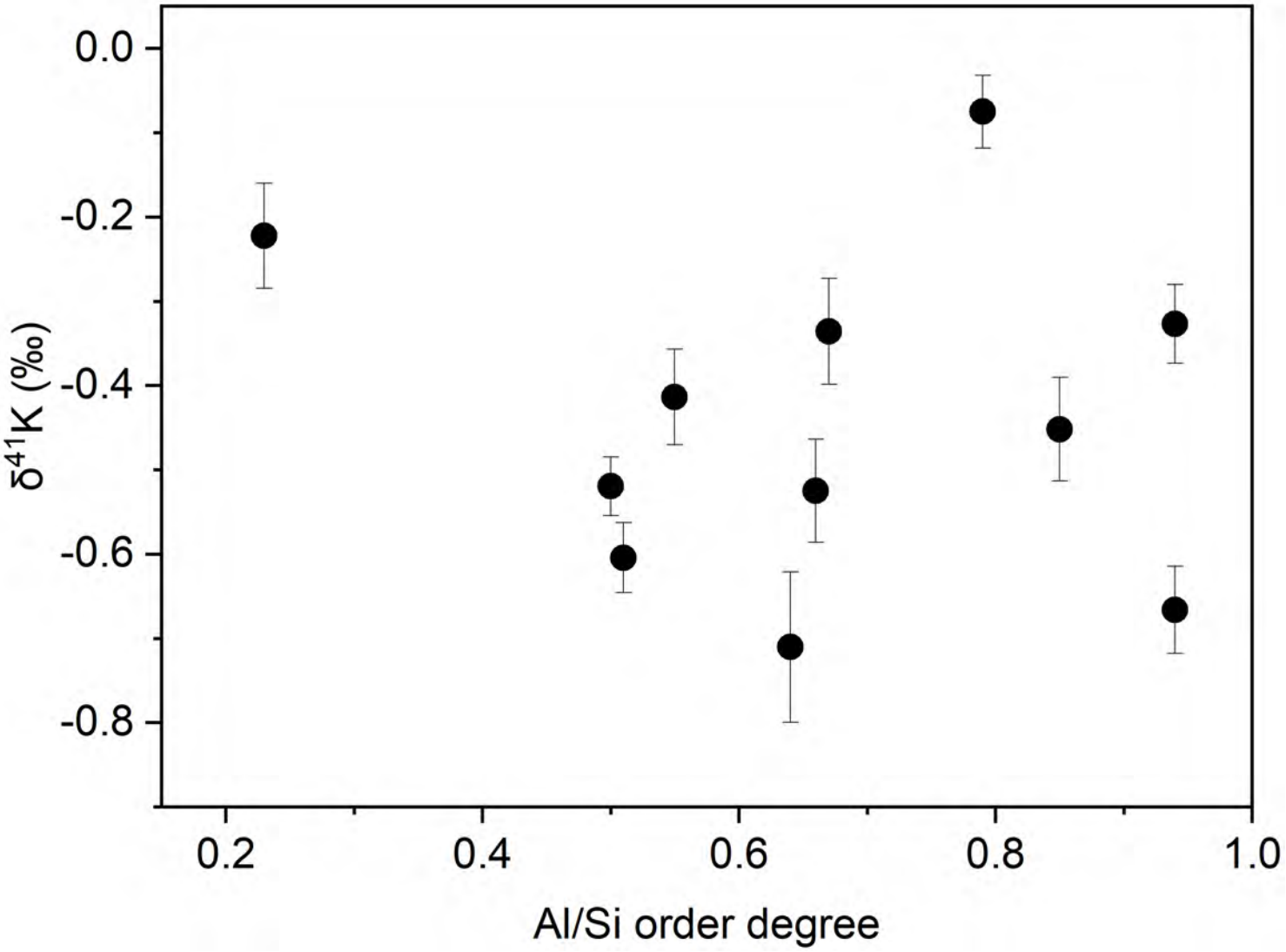

This is the peer-reviewed, final accepted version for American Mineralogist, published by the Mineralogical Society of America.
The published version is subject to change. Cite as Authors (Year) Title. American Mineralogist, in press.
DOI: https://doi.org/10.2138/am-2023-9006. http://www.minsocam.org/

**Fig. 4**

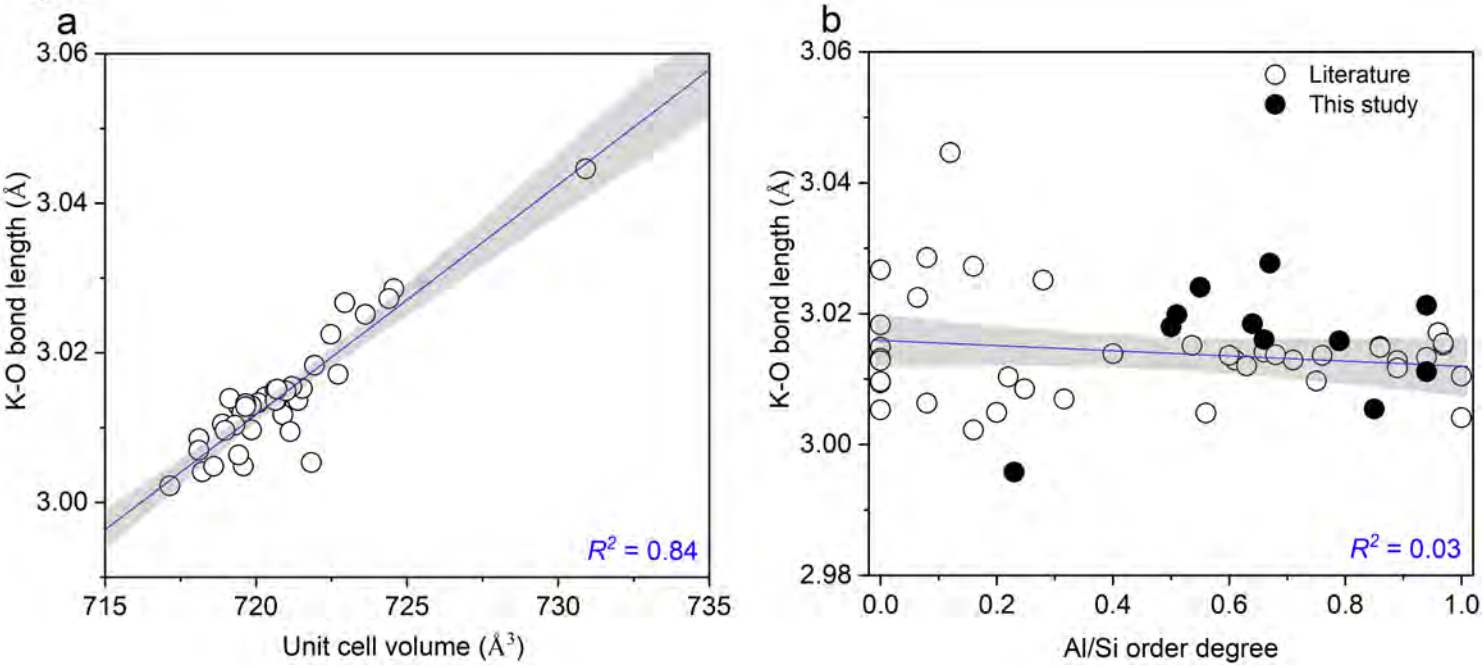

This is the peer-reviewed, final accepted version for American Mineralogist, published by the Mineralogical Society of America.
The published version is subject to change. Cite as Authors (Year) Title. American Mineralogist, in press.
DOI: https://doi.org/10.2138/am-2023-9006. http://www.minsocam.org/

**Fig. 5**

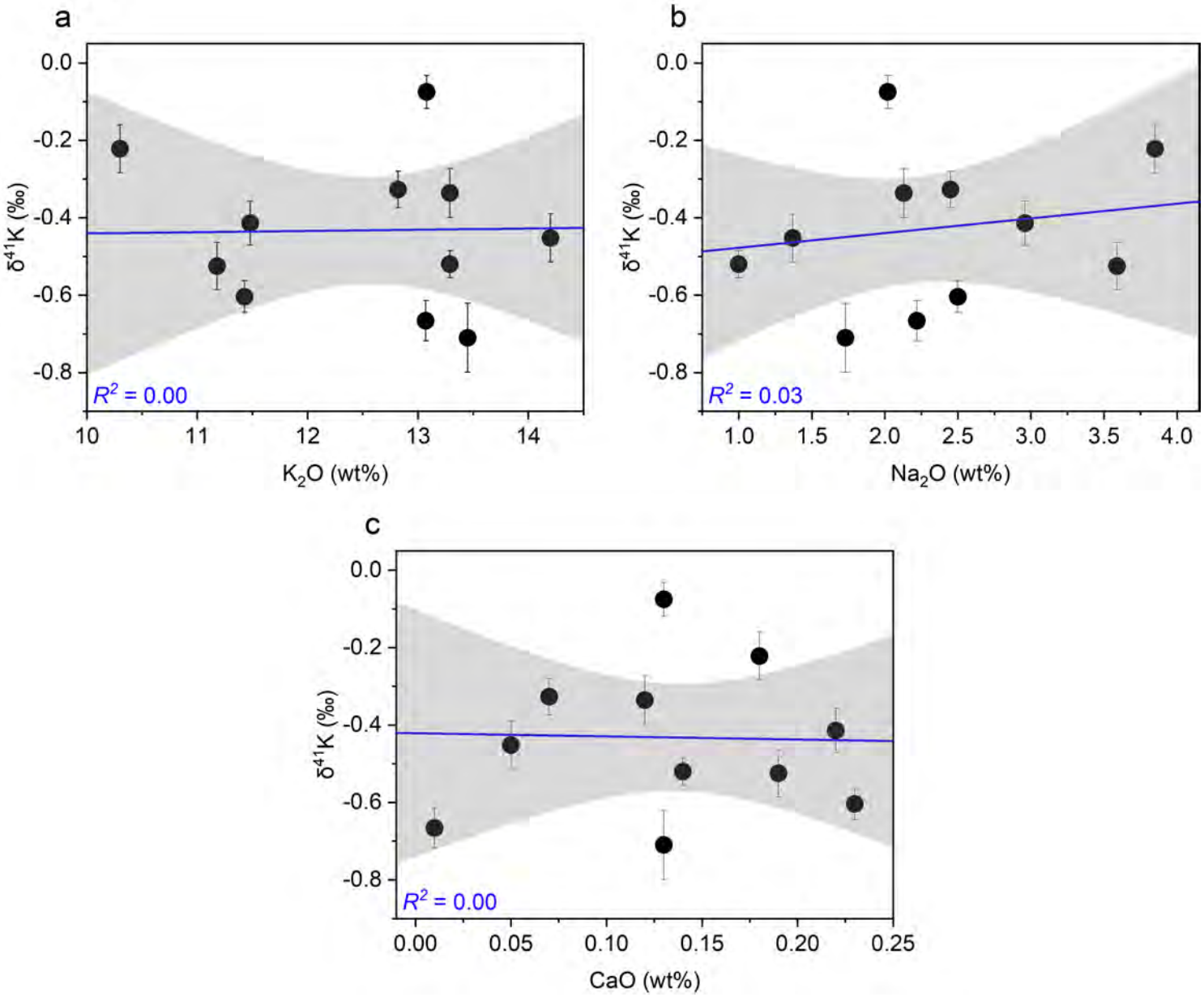

This is the peer-reviewed, final accepted version for American Mineralogist, published by the Mineralogical Society of America.
The published version is subject to change. Cite as Authors (Year) Title. American Mineralogist, in press.
DOI: https://doi.org/10.2138/am-2023-9006. http://www.minsocam.org/

**Fig. 6**

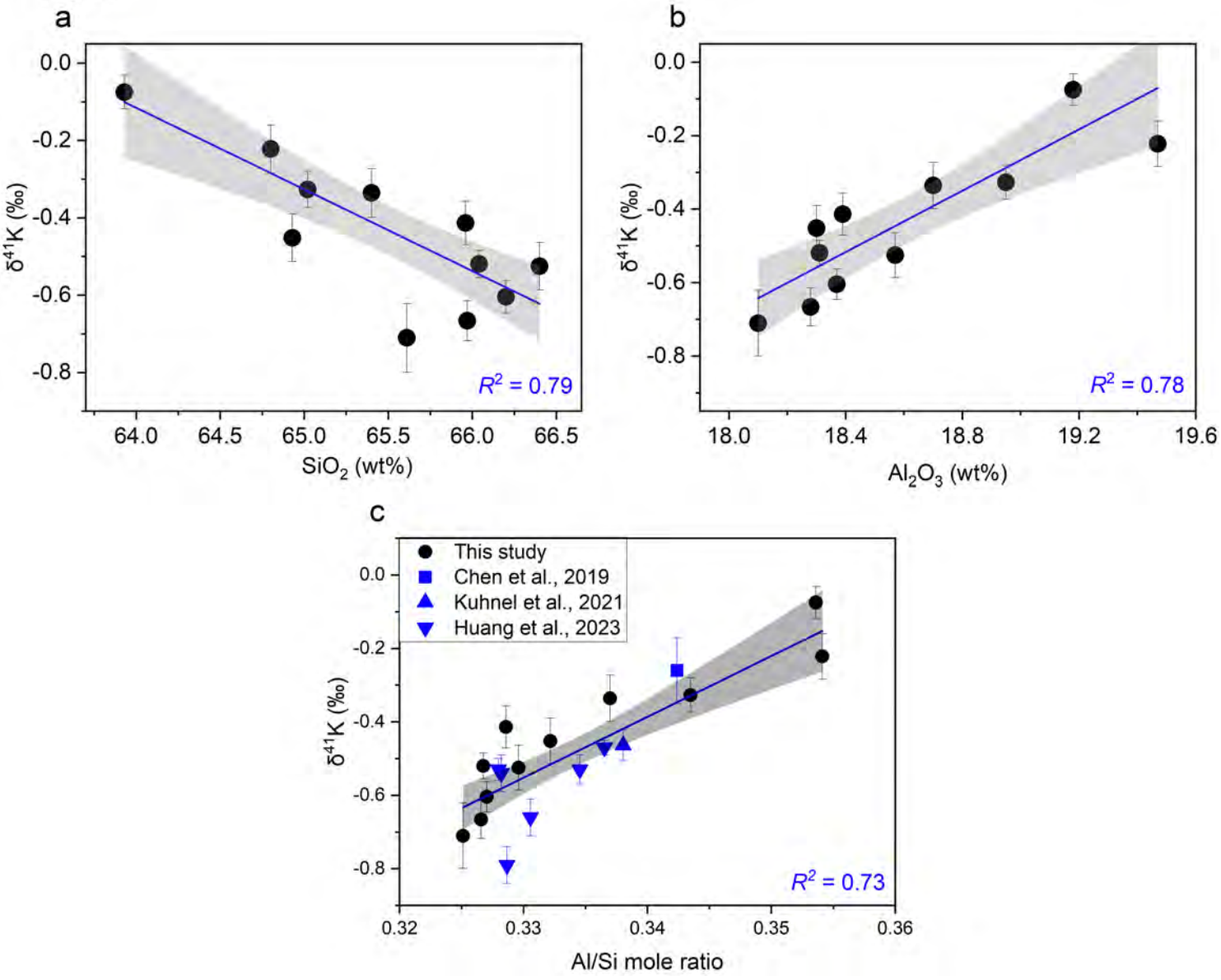

This is the peer-reviewed, final accepted version for American Mineralogist, published by the Mineralogical Society of America.
The published version is subject to change. Cite as Authors (Year) Title. American Mineralogist, in press.
DOI: https://doi.org/10.2138/am-2023-9006. http://www.minsocam.org/

**Fig. 7**

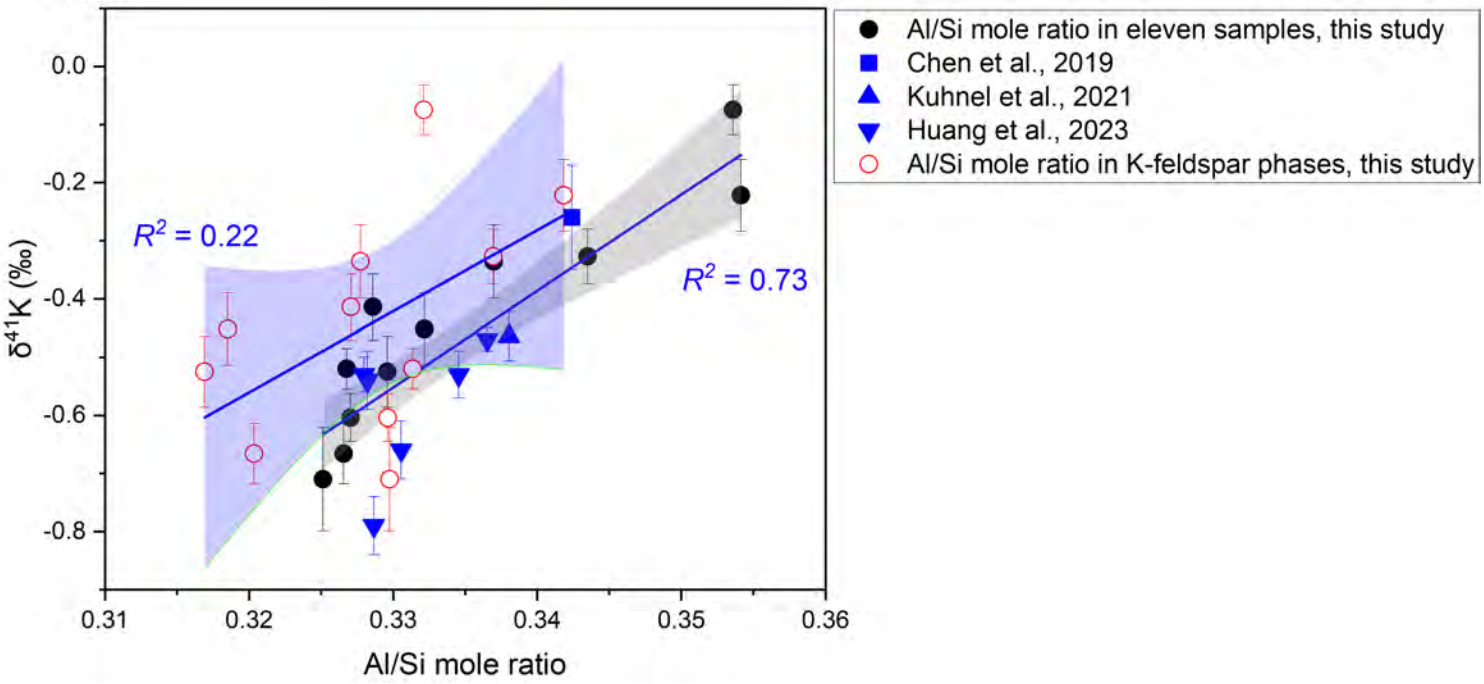

This is the peer-reviewed, final accepted version for American Mineralogist, published by the Mineralogical Society of America.
The published version is subject to change. Cite as Authors (Year) Title. American Mineralogist, in press.
DOI: https://doi.org/10.2138/am-2023-9006. http://www.minsocam.org/

**Fig. 8**

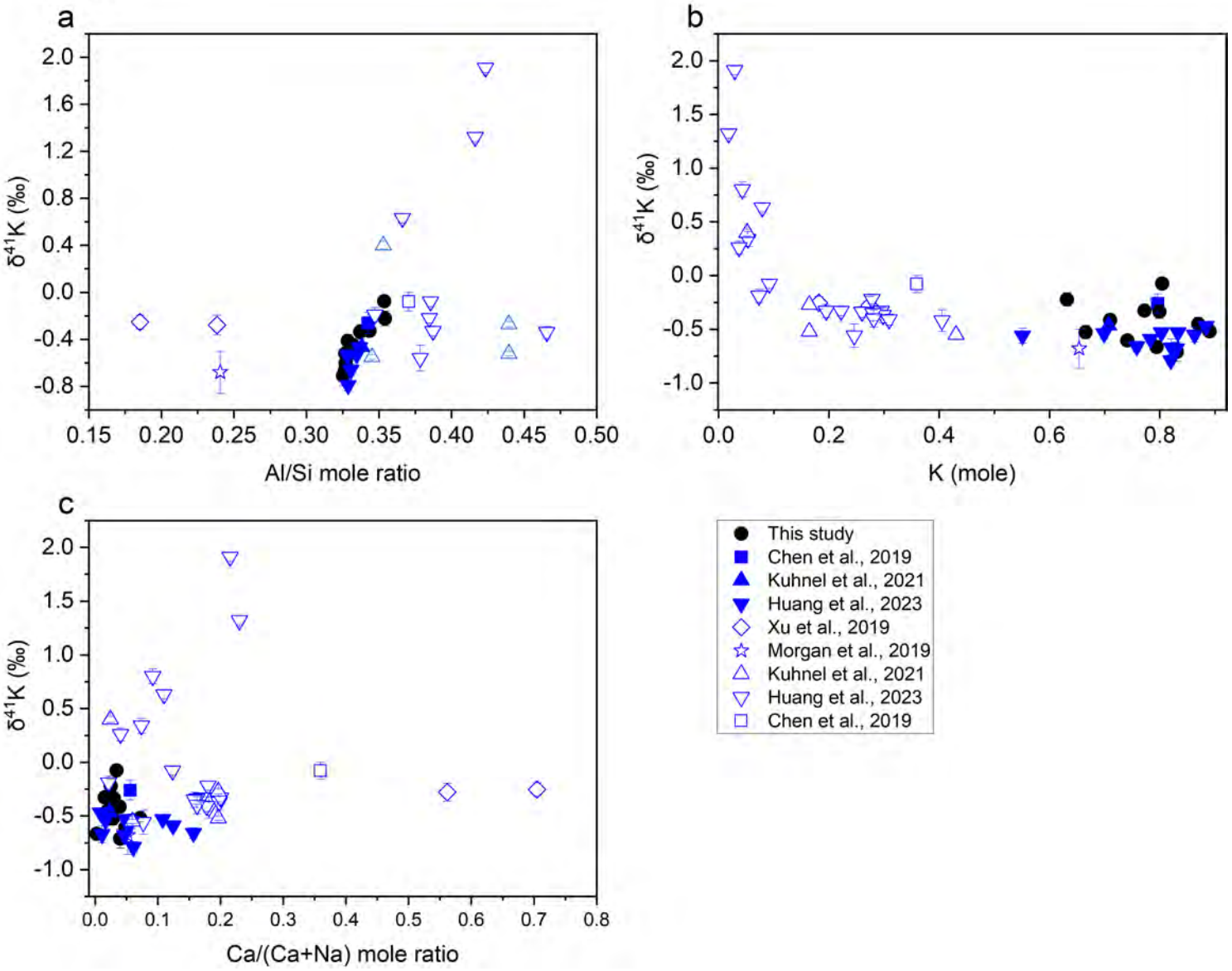

This is the peer-reviewed, final accepted version for American Mineralogist, published by the Mineralogical Society of America.
The published version is subject to change. Cite as Authors (Year) Title. American Mineralogist, in press.
DOI: https://doi.org/10.2138/am-2023-9006. http://www.minsocam.org/

**Fig. 9**

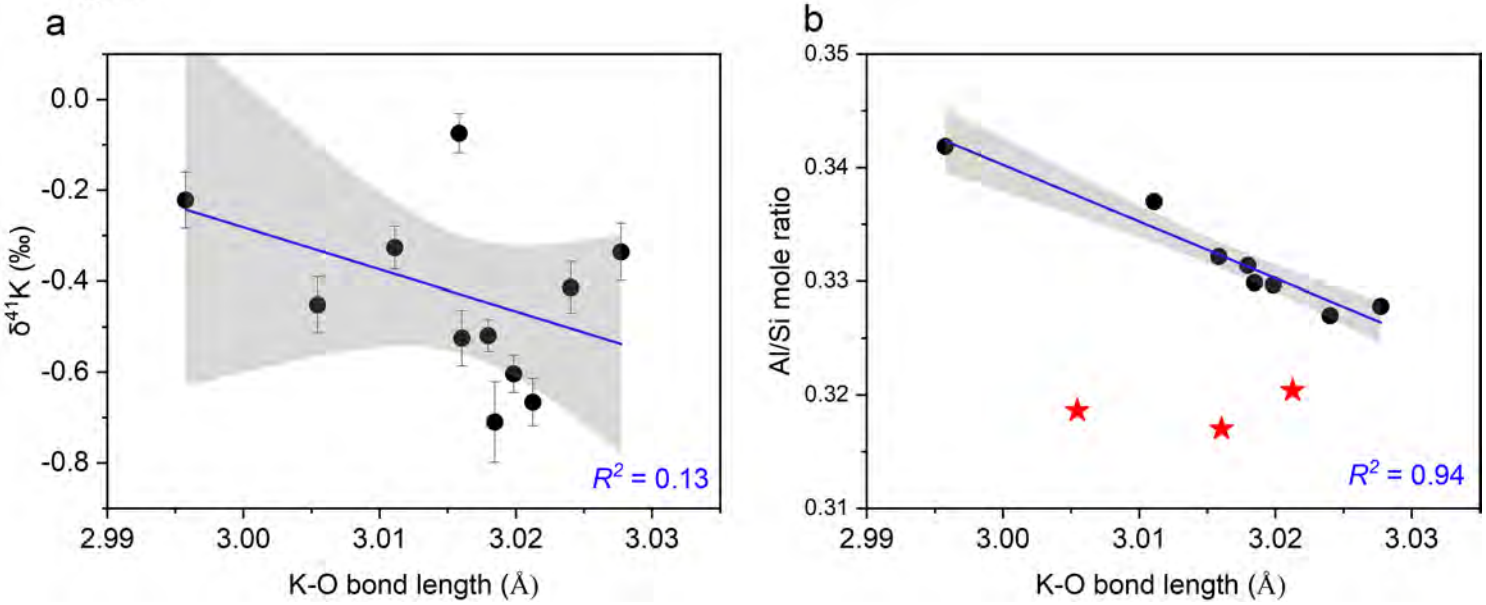

This is the peer-reviewed, final accepted version for American Mineralogist, published by the Mineralogical Society of America.
The published version is subject to change. Cite as Authors (Year) Title. American Mineralogist, in press.
DOI: https://doi.org/10.2138/am-2023-9006. http://www.minsocam.org/

**Fig. 10**